

Vertically Stacked Intraband Quantum Dot Devices for Mid-Wavelength Infrared Photodetection

Shihab Bin Hafiz, Mohammad M. Al Mahfuz, and Dong-Kyun Ko*

Cite This: *ACS Appl. Mater. Interfaces* 2021, 13, 937–943

Read Online

ACCESS |



Metrics & More



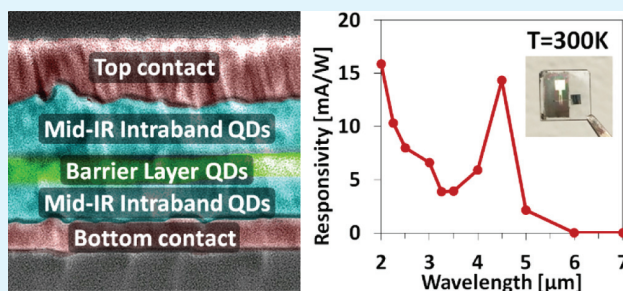
Article Recommendations



Supporting Information

ABSTRACT: Intraband quantum dots are degenerately doped semiconductor nanomaterials that exhibit unique optical properties in mid- to long-wavelength infrared. To date, these quantum dots have been only studied as lateral photoconductive devices, while transitioning toward a vertically stacked structure can open diverse opportunities for investigating advanced device designs. Here, we report the first vertical intraband quantum dot heterojunction devices composed of $\text{Ag}_2\text{Se}/\text{PbS}/\text{Ag}_2\text{Se}$ quantum dot stacks that bring the advantage of reduced dark conductivity with a simplified device fabrication procedure. We discuss the improvement in the colloidal synthesis of Ag_2Se quantum dots that are critical for vertical device fabrication, identify an important process that determines the mid-wavelength infrared responsivity of the quantum dot film, and analyze the basic device characteristics and key detector performance parameters. Compared to the previous generation of Ag_2Se quantum dot-based photoconductive devices, approximately 70 times increase in the mid-wavelength responsivity, at room temperature, is observed.

KEYWORDS: silver selenide, colloidal quantum dots, intraband, mid-wavelength infrared, barrier detector



INTRODUCTION

Today's thermal infrared sensing and imaging technologies are based on single-crystal or epitaxial semiconductors,^{1,2} while colloidal quantum dots (QDs) are emerging as alternative materials³ that capitalize on the benefits of cost-effectiveness and fabrication versatility. Among various libraries of QDs available to date, intraband QDs—a new subset of semiconductor QD material that utilizes optical transition between the first and second quantum-confined energy levels—have demonstrated their use in mid-wavelength infrared (MWIR = 3–5 μm) photodetection.^{4–11} In these intraband QDs, it has been studied that Auger recombination can be greatly suppressed,¹² owing to the QD's sparse density of state, thereby allowing higher temperature operation of infrared photodetectors. Achieving high operation temperature constitutes an important milestone for infrared sensors and imagers as it can remove the cryogenic cooling requirement, allowing photodetectors to be manufactured with reduced size, weight, power consumption, and cost. To date, MWIR intraband QD photodetectors have only been studied as lateral photoconductive devices,^{5,13} while advancing the device toward a vertically stacked structure can have great implications in their applications. Specifically, vertically stacked QD devices can enable direct integration of intraband QD technology with existing silicon read-out integrated circuits for fabricating focal plane arrays without hybridization.^{14,15} From a scientific point of view, the vertical structure enables the

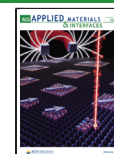
incorporation of complex heterostructure QD layer stacks that can be used to modulate carrier distribution and dynamics for improved detector performance.

Herein, we report the first vertical intraband QD heterojunction barrier devices composed of $\text{Ag}_2\text{Se}/\text{PbS}/\text{Ag}_2\text{Se}$ QD stacks. Ag_2Se QDs are unique heavy-metal-free intraband QDs that have tunable size-dependent optical absorption in the MWIR.¹⁰ Our group^{9,10} and others^{8,16} have recently investigated the device characteristics of Ag_2Se QD-based photoconductive photodetectors and have demonstrated appreciable room-temperature responsivity of 0.21 mA/W at 4.5 μm. Our vertical device design that incorporates PbS QDs as a barrier layer was inspired by the nBn (n-type/barrier/n-type) infrared photodetector design¹⁷ that has been adapted for InSb,¹⁸ HgCdTe,¹⁹ and InAs/GaSb superlattices.²⁰ The primary advantage of using a barrier layer in intraband QD-based devices is two-fold. First, the thin films composed of Ag_2Se QDs have been studied to have high electron concentration,^{9,21} giving rise to an extremely high dark conductivity that is detrimental to high sensitivity photo-

Received: November 2, 2020

Accepted: December 18, 2020

Published: December 29, 2020



detection. By introducing a potential barrier, dark conductivity can be significantly reduced. An ideal barrier structure that minimizes dark conductivity would be the one that is composed of both electron and hole barriers (resembling the p–i–n structure²²) to block the transport of thermally generated electrons and holes, respectively, while providing an unimpeded flow of photocarriers. In this study, we demonstrate the concept of hole barrier as it is immediately available using PbS QDs—a standard semiconductor QD that has been widely used in various QD optoelectronic applications.^{23–25} Second, implementing nBn barrier device structure greatly simplifies the device fabrication procedure. The fabrication is identical to creating a simple vertically stacked photoconductor via layer-by-layer QD deposition but with an inclusion of an additional QD layer that serves as a potential barrier.

In this paper, we describe the colloidal synthesis of Ag₂Se QDs with improved synthetic yield and discuss the device fabrication in which ligand exchange duration is found to be a critical parameter in creating MWIR-responsive QD films. Last, we carry out device characterization to understand carrier transport in QD stacks containing a barrier layer, measure the key detector performance parameters, and compare our results with other MWIR QD research reports.

RESULTS AND DISCUSSION

Compared to the lateral photoconductor devices, which require 2–3 QD film depositions, fabricating a vertically stacked device requires a large quantity of QDs to complete 20–30 layers of QD depositions. Thus, improving the existing QD synthesis yield was the first step toward achieving vertical devices since previously reported procedures^{9,26} suffer from very low synthetic yields (typically less than 3 mg for 25 mL volume reaction for QDs with sizes smaller than 5.5 nm or MWIR absorption peak less than 4.2 μm). It has been previously studied that pure tertiary phosphine chalcogenides, which are commonly used as precursors for metal chalcogenide QD synthesis, are rather unreactive with the metal precursors.^{27,28} A small addition of secondary phosphines, such as diphenylphosphine (DPP), is known to dramatically increase the synthetic yield. This has been discussed to be universal to all phosphine-based syntheses.²⁷ Following this protocol, we have added a small amount of DPP (TOP/DPP = 30:1 in volume) to our synthesis and observed 10-fold increase in our 5.5 nm Ag₂Se QD synthesis yield (50 mg for 55 mL volume reaction) without sacrificing the QD size uniformity. Figure 1a shows a transmission electron microscopy (TEM) image of the as-synthesized Ag₂Se QDs with an average size of 5.5 nm and size dispersion of approximately 35%. PbS QDs, which will be used as a barrier layer, were synthesized following the previously reported protocol,²⁹ and the TEM image (average size = 5 nm, size dispersion = 20%) of the sample is shown in Figure 1b. Figure 1c shows the Fourier transform infrared (FTIR) spectrum of Ag₂Se QDs, which shows a distinct intraband absorption peak at 4.2 μm . Other characteristic peaks around 3.4, 4.4, and 6.8 μm correspond to vibrational modes of C–H, CO₂, and trioctylphosphine (TOP), respectively. PbS QDs show interband absorption peak centered at 1200 nm, as shown in Figure 1d.

To fabricate the device, we started with a sapphire substrate prepatterned with a Ag electrode that serves as a bottom Ohmic contact. The Ag₂Se QD layers were then deposited by repeating layer-by-layer QD deposition and 1,2-ethanedithiol

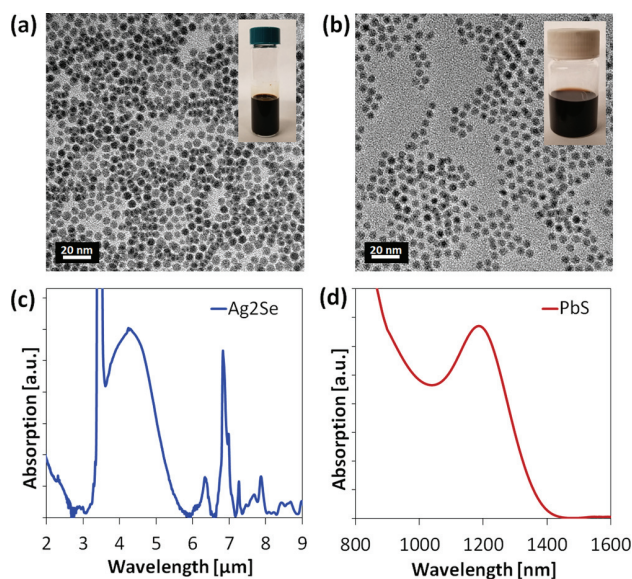


Figure 1. Characterization of Ag₂Se and PbS QDs. (a) TEM image of Ag₂Se QDs, (b) TEM image of PbS QDs. The insets in (a,b) show photographs of the synthesized Ag₂Se and PbS QDs suspended in an organic solvent, respectively. (c,d) Optical absorption spectra of the as-synthesized Ag₂Se and PbS QDs, respectively.

(EDT) ligand exchange procedure^{30,31} to create an electronically coupled QD film. After 10 rounds of Ag₂Se QD layer deposition, a PbS QD barrier layer (4–5 depositions) was deposited following the identical procedure used for Ag₂Se QDs. The QD device layer was completed by adding another 10 layers of Ag₂Se QDs. Optimization of the QD spin-coating process was critical in achieving a crack-free QD film (see the Supporting Information S1). For the top contact, 120 nm of Ag with two finger electrodes was deposited using a shadow mask. In conjunction with the bottom electrode, this defines the device optical area of 200 \times 200 μm , as shown in Figure 2a. To increase the carrier collection in this top-via opening, Ag nanowires^{32,33} were spin-coated using diluted nanowire solution and processed to enhance the nanowire-to-nanowire electrical connection (junction soldering), before depositing the Ag top contact. The nanowire layer serves as an infrared transparent contact, exhibiting 73% transmission in MWIR with a low sheet resistance of 29 Ω/sq (see the Supporting Information S2). The device cross-section, examined using a scanning electron microscope is shown in Figure 2b. The total QD layer thickness was approximately 300 nm (120 nm Ag₂Se, 60 nm PbS, and 120 nm Ag₂Se QDs).

A critical step in fabricating a MWIR-responsive QD device was optimizing the EDT–ligand exchange duration which was found to have a narrow temporal window. We carried out a systematic investigation of the QD ligand exchange by fabricating a series of devices with ligand exchange duration varying from 0 to 80 s and measuring the device responsivity by illuminating the devices with 4.5 μm radiation. As shown in Figure 2c, the infrared responsivity rises and decays rapidly around 10 to 50 s, where a peak is reached at 30 s. Outside this region, around 0 s, QDs in the device are not sufficiently coupled, leading to a device resistance on the order of tens of M Ω . Above 60 s, optical absorption in the MWIR weakens (see the Supporting Information S3) due to reduced electron concentration^{9,34} and we observe a complete absence of device

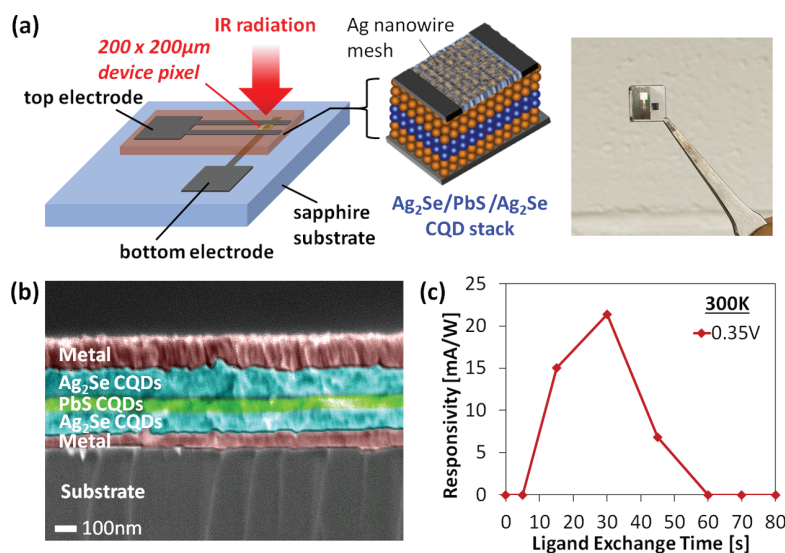


Figure 2. Fabrication of vertically stacked QD barrier devices. (a) Schematic of the device structure and photograph of a fabricated device. (b) False color cross-sectional SEM image of the device showing the sapphire substrate, bottom contact (Ag), QD layers, and top contact (Ag). (c) Responsivity at $4.5 \mu\text{m}$ plotted as a function of EDT ligand exchange duration.

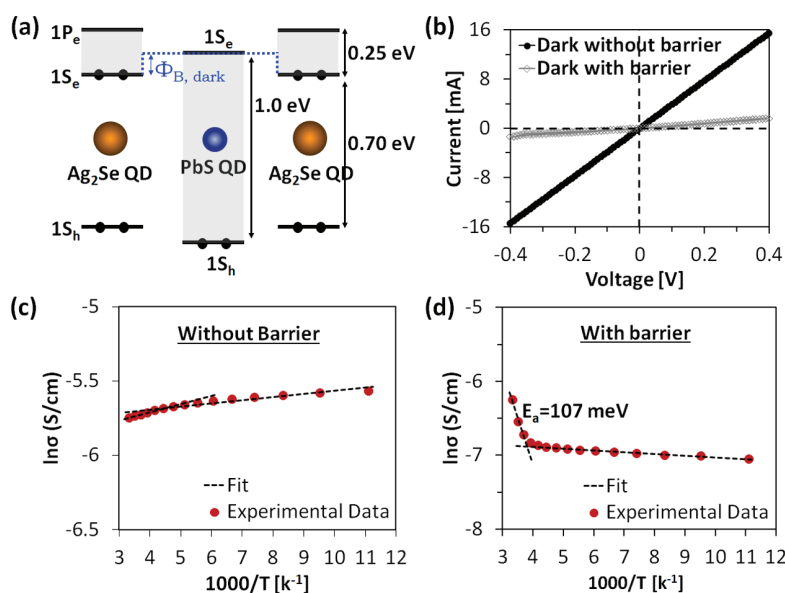


Figure 3. Electrical characterization of $\text{Ag}_2\text{Se}/\text{PbS}/\text{Ag}_2\text{Se}$ QD nBn devices. (a) Schematic of the energy-level alignment of $\text{Ag}_2\text{Se}/\text{PbS}/\text{Ag}_2\text{Se}$ QD estimated from refs.^{8,35} $1S_h$, $1S_e$, and $1P_e$ denote first valence energy level, first conduction energy level, and second conduction energy level, respectively. The blue dotted line shows the $1S_e$ Ag_2Se QD– $1S_e$ PbS QD conduction offset which serves as a potential barrier (denoted as Φ_B , extracted from our measurements to be 107 meV) for electrons under dark. (b) Current–voltage characteristics obtained under the dark from devices with and without a PbS QD barrier layer. (c,d) Temperature-dependent dark conductivity obtained from device without and with a barrier layer, respectively.

MWIR responsivity. The ligand exchange of Ag_2Se QD films seems to involve a complex interplay²¹ of surface chemistry, optoelectronic property, and physical microstructure of the QD film, as discussed more below.

Prior to the photodetector characterization, we carried out basic electrical measurements of our fabricated devices. Figure 3a shows the energy-level diagram estimated from prior photoemission spectroscopy measurement reports on similarly sized PbS³⁵ and Ag_2Se ⁸ QDs where, in degenerated-doped intraband Ag_2Se QD, $1S_e$ serves as a valence level (ground state) and $1P_e$ serves as conduction level (excited state). An

energy-level offset is created by PbS QD, which creates a potential barrier (denoted as Φ_B) for electrons under dark conditions (see the Supporting Information S4 for more details). This is evident in Figure 3b where the device resistance increases by 800% through the insertion of the PbS QD barrier layer. The uniqueness of nBn device design arises from the fact that the metal contact properties do not change with the insertion of the barrier layer since the metals are in contact with the bottom and top n- Ag_2Se QD layers even for barrier devices. This is in agreement with the data in Figure 3b, where the dark current–voltage (I – V) characteristics of

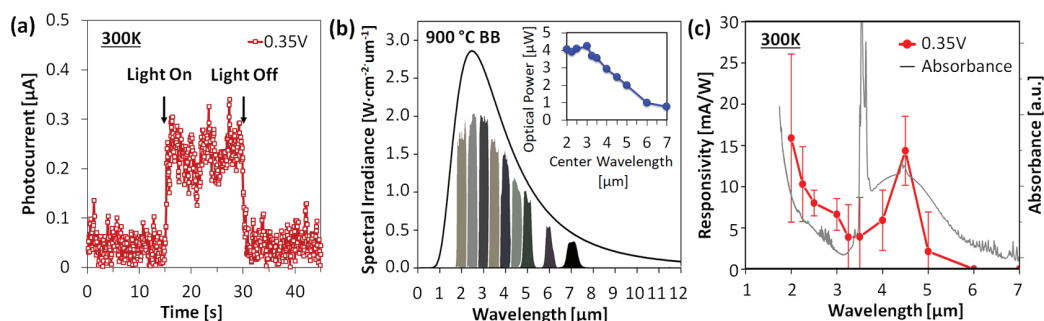


Figure 4. Photodetector characterization of $\text{Ag}_2\text{Se}/\text{PbS}/\text{Ag}_2\text{Se}$ QD nBn devices. (a) Photocurrent measurements carried out using Ge-filtered 900 °C blackbody illumination. (b) Spectral irradiance of 900 °C blackbody estimated from Planck radiation formula. The inset shows the optical power when a series of band pass filters, having center wavelength varying from 2 to 7 μm , was used to spectrally separate the infrared illumination. Each optical power was calculated from respective shaded area under the spectral irradiance curve and was corrected for source aperture, optical pass, optics, and detector area. (c) Spectral responsivity measured from barrier devices. The data plot was obtained from 5 devices, and variations are represented with error bars. Optical absorbance spectra of Ag_2Se CQD film after ligand exchange is overlaid with the spectral response plot. All measurements were conducted at room temperature 300 K with 0.35 V bias at 15 Hz.

devices with the barrier layer maintain Ohmic behavior, similar to the I - V obtained from devices without the barrier layer (metal- Ag_2Se QDs-metal photoconductor; see the [Supporting Information S5](#) for details). In comparison, if the device was designed to be nB or Bn structure, a new metal-barrier layer contact will be formed, and it has been reported that silver (metal) and PbS QDs form Schottky contacts.³⁶

To better understand the carrier transport in these devices, temperature-dependent conductivities were measured, as shown in [Figure 3c](#). In a typical semiconductor QD film, the conductivity can be expressed as³⁷

$$\sigma = qN_C \exp\left[\frac{-(E_C - E_F)}{KT}\right] \mu_0 \exp\left(\frac{-E_\mu}{KT}\right) \exp\left(-\frac{E_\Phi}{KT}\right)$$

where q is the elementary charge, N_C is the effective conduction density of states, E_C is the conduction level, E_F is the Fermi level, and μ_0 is the mobility prefactor. Following this equation, there are three thermal activation energies: $(E_C - E_F)$ related to carrier generation, hopping mobility term E_μ , and E_Φ associated with the presence of potential barrier (for barrier devices). In heavily doped n-type intraband QDs, $(E_C - E_F)$ term can be neglected since the Fermi energy level is positioned close to (or above) the conduction level. Furthermore, for devices without a barrier, shown in [Figure 3c](#), a positive slope from 300 to 230 K is observed. This implies that thermally activated hopping is not the transport mechanism. It is plausible that QD necking (while maintaining quantum confinement; see the [Supporting Information S3](#)) may have taken place during the ligand-exchange process.^{38,39} This indicates that the activation energy of hopping mobility, which arises from energy site variations (QD size non-uniformity)^{40,41} can be neglected. The slope from 300 to 230 K in [Figure 3d](#) is then predominantly related to the energetic height of the potential barrier in nBn devices. From this measurement analysis, the height of the electron potential barrier in the dark is estimated to be $\Phi_B = 107$ meV as denoted in [Figure 3a](#). At around 250 K, we observe a change in the slope in [Figure 3c](#) which is also observed in devices with the barrier ([Figure 3d](#)). This is expected to be associated with the change in the charge transport mechanism in Ag_2Se QD layers at low temperatures and warrants further study.^{42,43}

Photocurrent measurements were conducted by illuminating the device with a calibrated blackbody heated at 900 °C. The

blackbody radiation was chopped at 15 Hz and filtered through Ge which only allows mid- to long-wavelength infrared photons (wavelength longer than 1.8 μm) to pass through. The device photocurrent was measured using a preamplifier and lock-in technique. [Figure 4a](#) shows the photocurrent measured from our QD nBn devices at room temperature. A distinct photoresponse was observed with a photocurrent corresponding to 0.23 μA at 0.35 V of applied bias (see the [Supporting Information S6](#) for more details). It should be noted that, for devices without the barrier, photocurrent measurement was not possible due to the high electrical conductivity (3.2×10^{-3} S cm^{-1}) of the device.

To investigate the detailed photoresponse in the technologically important atmospheric transmission window of 3–5 μm , spectral responsivity measurements were carried out using a set of Fabry–Perot band-pass filters, having center wavelengths (CTs) varying from 2 to 7 μm ([Figure 4b](#)). [Figure 4c](#) shows the spectral responsivity of our $\text{Ag}_2\text{Se}/\text{PbS}/\text{Ag}_2\text{Se}$ QD nBn devices measured without cooling. A good agreement in the spectral shape of our responsivity data and optical absorption of Ag_2Se QDs indicates that the measured photoresponse arises from our Ag_2Se QDs. Compared to our previous work on planar photoconductive photodetectors,⁹ the room-temperature responsivity at 3–5 μm was improved by approximately 70 times. This is mainly attributed to the shorter distance (300 nm) that the photogenerated carriers have to travel in vertical QD-stack devices compared to the 10 μm transport gap in planar photoconductors. The peak responsivity of 13.3 mA/W was measured at 4.5 μm , which corresponds to an external quantum efficiency (EQE) of 0.36%. It is expected that EQE can be improved by increasing light absorption, which can be achieved by developing thicker Ag_2Se QD films or employing other optical trapping strategies.⁶

Performance of a photodetector is characterized by the specific detectivity, given as

$$D^* = \frac{R \sqrt{AB}}{I_N} = \frac{R \sqrt{A}}{i_n}$$

where A is the detector area, B is the bandwidth, I_N is the noise current, i_n is the noise current density, and R is the responsivity. The i_n of our QD barrier device was measured using a closed shield at 300 K with a spectrum analyzer where a low-noise preamplifier was used to apply a bias of 0.35 V.

Table 1. Summary of Photodetector Performance Parameters of Ag₂Se/PbS/Ag₂Se QD Barrier Devices and Comparison to Other Representative Research Works^a

<i>T</i> [K]	QD material (type of absorption)	λ_{peak} [μm]	<i>R</i> [mA/W]	i_{n} [pA Hz ^{-1/2}]	<i>D</i> * [Jones]	device structure	refs
85	HgTe (interband)	4.5	1620	0.07	4×10^{11}	photodiode	44
138	HgTe (interband)	4	81	0.7	1.1×10^{10}	photodiode	45
80	HgTe (interband)	4.8	230	0.1	5.4×10^{10}	photoconductor	46
300	HgSe (intraband)	6	800	10^3	10^8	photoconductor	5
80	HgSe (intraband)	5	0.13	1	2.6×10^7	photoconductor	13
80	HgSe (intraband)	4.4	0.1	0.1	1.5×10^9	CQDIP	47
300	Ag ₂ Se (intraband)	4.5	13.3	10^3	3×10^5	barrier device	(this study)

^a*T*, λ_{peak} , *R*, i_{n} , and *D** denote measurement temperature, peak wavelength, responsivity, noise current density, and specific detectivity, respectively.

The measured value at 15 Hz with 1 Hz bandwidth was 10^{-9} A Hz^{-1/2}, which is similar to the earlier report on intraband HgSe QD photoconductors.⁵ Recent literature on HgSe QDs with improved size dispersion reports i_{n} as low as 1 pA Hz^{-1/2} measured at 80 K.¹³ With the responsivity of 13.3 mA/W at 4.5 μm , our device exhibits a specific detectivity of 3×10^5 Jones at 300 K. Table 1 summarizes the performance parameters of our current generation QD barrier devices, along with the comparison to other representative research works. Here, we have included the performance of the interband HgTe QD devices (photoconductor and photodiodes), which is currently the leading MWIR QD material.

CONCLUSIONS

In summary, we have presented the QD synthesis, device fabrication, and detector characterization of vertically stacked nBn devices using intraband Ag₂Se QDs as the MWIR absorber and PbS QDs as a barrier layer. An 800% increase in the dark resistivity and 70-fold improvement in the MWIR responsivity were measured, compared to the lateral photoconductive devices. The energy-level diagram (Figure 3a) constructed from our measurement analysis suggests that further performance improvements are possible via optimizing the barrier height. An ideal nBn structure would have a potential barrier that minimizes the transport of dark carriers while simultaneously maximizing the flow of photocarriers. This places the optimal $1S_{\text{e}}$ level of PbS QDs to the same energetic position of $1P_{\text{e}}$ of Ag₂Se QDs. More improvements are anticipated by having complementary electron and hole barriers or by incorporating other advanced device designs such as multiple quantum wells that can be fabricated by stacking alternating QD layers vertically.⁴⁷ Hence, the QD stack device demonstrated here provides a versatile platform, and its impact may outreach many areas of optoelectronics, including emitters and lasers.

METHODS

Chemicals. TOP (Sigma-Aldrich, 90%), oleylamine (Sigma-Aldrich, 70%), selenium (Sigma-Aldrich, 99.999%), silver chloride (Sigma-Aldrich, 99%), lead oxide (Aldrich, 99.999%), 1-octadecene (Aldrich, 90%), oleic acid (Aldrich, 90%), hexamethyldisilathiane (Aldrich, synthesis grade), EDT (Fluka, >98.0%), 1-butanol (Sigma-Aldrich, 99.8%), hexane (Sigma-Aldrich, 98.5%), methanol (Sigma-Aldrich, 99.8%), octane (Sigma-Aldrich, 99%), and ethyl alcohol (Sigma-Aldrich, 99.5%) were used as received without further purification.

Ag₂Se QD Synthesis. Ag₂Se QDs having an absorption peak at 4.2 μm were synthesized using a standard hot-injection technique.^{9,26} Selenium and silver precursor solutions were prepared inside a nitrogen-filled glovebox by dissolving Se powder in TOP (1 M) and dissolving AgCl in TOP (0.5 M). 30 mL of oleylamine was transferred

to a three-neck flask and heated to 90 °C under vacuum for 1 h. After switching to nitrogen, 8 mL of 1 M TOP-Se was injected, and the temperature was raised to 130 °C. Then, 16 mL of 0.5 M TOP-Ag mixed with 800 μL DPP was injected to initiate a reaction. The reaction was terminated after 20 s by injecting 20 mL of butanol and cooling in a water bath. The QDs were then purified with a mixture of ethanol and methanol, followed by centrifugation. The final QDs were dispersed in octane (30 mg/mL) after three methanol washes.

PbS QD Synthesis. The synthesis of PbS QDs with an absorption peak at 1200 nm was conducted following the previously reported procedure.²⁹ Lead oxide (0.45 g) was dissolved in 10 mL of 1-octadecene and 4 mL of oleic acid. The solution was kept in a vacuum for 2 h at 110 °C in a three-neck flask. Then, 0.2 mL of hexamethyldisilathiane diluted with 10 mL of 1-octadecene (dry) was injected to initiate reaction at 150 °C. The temperature was maintained at 120 °C for 4 min. The synthesis was terminated with a water bath, precipitated using ethanol by centrifugation inside a glovebox. The final QDs were redispersed in a mixture of hexane/octane (30 mg/mL).

Device Fabrication. QD-based nBn devices were fabricated using sapphire substrates. A bottom contact of 80 nm (Cr/Ag) was deposited using thermal evaporation via a shadow mask. Ag₂Se and PbS QDs were deposited by spin coating (2000 rpm, 30 s) and performing EDT (0.1 M in methanol) ligand-exchange. A total of 20 layers of Ag₂Se QDs were deposited, where 4–5 layers of PbS QDs were deposited after the first 10 layers of Ag₂Se QDs. Ag NW solution, diluted by 10 in isopropyl alcohol, was spin-coated (2000 rpm, 30 s) on top of the QD film and exposed to water vapor for 3–5 s, followed by drying for 30 s in air. Then, 120 nm Ag was thermally evaporated using a shadow mask to complete the top contact. The bottom contact pad was exposed by cleaning off the QD film using a wooden tip.

Device Characterization. Optical absorption of Ag₂Se QD films was measured using a Thermo Nicolet 370 FTIR spectrometer. Non-ligand exchanged and ligand-exchanged QD films were prepared on KBr and ZnSe discs, respectively. Ligand-exchange was performed following the identical procedure described for device fabrication. Optical absorption spectra of PbS QDs (dissolved in tetrachloroethylene) were obtained using StellarNet UV-Vis-NIR spectrometer (RW-NIRX-SR and BLK-CXR). TEM images were obtained using JEOL JEM-F200. A SEM image was acquired using JEOL JSM-7900F. An Agilent 4155 semiconductor parameter analyzer was used for current–voltage measurements. An MMR Joule–Thomson refrigerator chamber was used for the temperature-dependent dark *I*–*V* measurements, where the device was mounted inside the vacuum chamber (30 mTorr), and the temperature was controlled using an MMR K2000.

Photodetector Parameter Measurements. Photocurrent was measured by illuminating the device with a calibrated blackbody heated at 900 °C. A chopper was used to modulate the blackbody radiation at 15 Hz, where the light was filtered through Ge. The device-to-source distance was 13.5 cm. A preamplifier (SR570) coupled with a lock-in amplifier (SR830) was used to measure the photocurrent. The preamplifier also provided a bias of 0.35 V. Similarly, spectral responsivity was measured replacing the Ge with a

set of Fabry–Perot band-pass filters, having center wavelengths varying from 2 to 7 μm . For the noise current density measurements, SR760 spectrum analyzer was used at 15 Hz with SR570 preamplifier providing a low-noise bias. The preamplifier, spectrum analyzer, and the device were kept inside a Faraday cage to avoid any kind of external noise, and all instruments were grounded.

■ ASSOCIATED CONTENT

SI Supporting Information

The Supporting Information is available free of charge at <https://pubs.acs.org/doi/10.1021/acsami.0c19450>.

Optical image of QD film surface, SEM image and properties of Ag nanowire network, optical absorption spectra, energy level diagram, I – V characteristics, and photocurrent measurements (PDF)

■ AUTHOR INFORMATION

Corresponding Author

Dong-Kyun Ko – Department of Electrical and Computer Engineering, New Jersey Institute of Technology, Newark, New Jersey 07102, United States; orcid.org/0000-0003-1834-0241; Email: dkko@njit.edu

Authors

Shihab Bin Hafiz – Department of Electrical and Computer Engineering, New Jersey Institute of Technology, Newark, New Jersey 07102, United States

Mohammad M. Al Mahfuz – Department of Electrical and Computer Engineering, New Jersey Institute of Technology, Newark, New Jersey 07102, United States

Complete contact information is available at: <https://pubs.acs.org/doi/10.1021/acsami.0c19450>

Notes

The authors declare no competing financial interest.

■ ACKNOWLEDGMENTS

This work was supported by US National Science Foundation under grant ECCS-1809112.

■ REFERENCES

- (1) Rogalski, A. Infrared Detectors: An Overview. *Infrared Phys. Technol.* **2002**, *43*, 187–210.
- (2) Downs, C.; Vandervelde, T. Progress in Infrared Photodetectors since 2000. *Sensors* **2013**, *13*, 5054–5098.
- (3) Rogalski, A.; Kopytko, M.; Martyniuk, P. Comparison of Performance Limits of HOT HgCdTe Photodiodes and Colloidal Quantum Dot Infrared Detectors. *Proceedings of SPIE Infrared Technology and Applications*, 2020; Vol. 11407, p 114070V.
- (4) Deng, Z.; Jeong, K. S.; Guyot-Sionnest, P. Colloidal Quantum Dots Intraband Photodetectors. *ACS Nano* **2014**, *8*, 11707–11714.
- (5) Lhuillier, E.; Scarafagio, M.; Hease, P.; Nadal, B.; Aubin, H.; Xu, X. Z.; Lequeux, N.; Patriarche, G.; Ithurria, S.; Dubertret, B. Infrared Photodetection Based on Colloidal Quantum-Dot Films with High Mobility and Optical Absorption up to THz. *Nano Lett.* **2016**, *16*, 1282–1286.
- (6) Tang, X.; Wu, G. F.; Lai, K. W. C. Plasmon Resonance Enhanced Colloidal HgSe Quantum Dot Filterless Narrowband Photodetectors for Mid-Wave Infrared. *J. Mater. Chem. C* **2017**, *5*, 362–369.
- (7) Lan, X.; Chen, M.; Hudson, M. H.; Kamysbayev, V.; Wang, Y.; Guyot-Sionnest, P.; Talapin, D. V. Quantum Dot Solids Showing State-Resolved Band-Like Transport. *Nat. Mater.* **2020**, *19*, 323–329.
- (8) Qu, J.; Goubet, N.; Livache, C.; Martinez, B.; Amelot, D.; Gréboval, C.; Chu, A.; Ramade, J.; Cruguel, H.; Ithurria, S.; Silly, M. G.; Lhuillier, E. Intraband Mid-Infrared Transitions in Ag₂Se

Nanocrystals: Potential and Limitations for Hg-Free Low-Cost Photodetection. *J. Phys. Chem. C* **2018**, *122*, 18161–18167.

(9) Hafiz, S. B.; Scimeca, M. R.; Zhao, P.; Paredes, I. J.; Sahu, A.; Ko, D.-K. Silver Selenide Colloidal Quantum Dots for Mid-Wavelength Infrared Photodetection. *ACS Appl. Nano Mater.* **2019**, *2*, 1631–1636.

(10) Hafiz, S. B.; Scimeca, M. R.; Sahu, A.; Ko, D.-K. Mid-Infrared Colloidal Quantum Dot Based Nanoelectronics and Nano-Optoelectronics. *ECS Trans.* **2019**, *92*, 11–16.

(11) Ramiro, I.; Özdemir, O.; Christodoulou, S.; Gupta, S.; Dalmases, M.; Torre, I.; Konstantatos, G. Mid-And Long-Wave Infrared Optoelectronics via Intraband Transitions in PbS Colloidal Quantum Dots. *Nano Lett.* **2020**, *20*, 1003–1008.

(12) Melnychuk, C.; Guyot-Sionnest, P. Auger Suppression in n-Type HgSe Colloidal Quantum Dots. *ACS Nano* **2019**, *13*, 10512–10519.

(13) Chen, M.; Shen, G.; Guyot-Sionnest, P. Size Distribution Effects on Mobility and Intraband Gap of HgSe Quantum Dots. *J. Phys. Chem. C* **2020**, *124*, 16216–16221.

(14) Klem, E. J. D.; Gregory, C.; Temple, D.; Lewis, J. PbS Colloidal Quantum Dot Photodiodes for Low-Cost SWIR Sensing. *Proc. SPIE* **2015**, *9451*, 945104.

(15) Temple, D. S.; Hilton, A.; Klem, E. J. D.; Towards Low-Cost Infrared Imagers: How to Leverage Si IC Ecosystem. *Proceedings of SPIE Technologies for Optical Countermeasures XIII*, 2016; Vol. 9989, p 99890E.

(16) Park, M.; Choi, D.; Choi, Y.; Shin, H.-b.; Jeong, K. S. Mid-Infrared Intraband Transition of Metal Excess Colloidal Ag₂Se Nanocrystals. *ACS Photonics* **2018**, *5*, 1907–1911.

(17) Martyniuk, P.; Kopytko, M.; Rogalski, A. Barrier Infrared Detectors. *Opto-Electron. Rev.* **2014**, *22*, 127–146.

(18) Evirgen, A.; Perez, J. P.; Christol, P.; Cordat, A.; Nedelcu, A.; Abautret, J. Midwave Infrared InSb nBn Photodetector. *Electron. Lett.* **2014**, *50*, 1472–1473.

(19) Kopytko, M.; Kębłowski, A.; Gawron, W.; Madejczyk, P.; Kowalewski, A.; JóÅwikowski, K. High-Operating Temperature MWIR nBn HgCdTe Detector Grown by MOCVD. *Opto-Electron. Rev.* **2013**, *21*, 402–405.

(20) Rodriguez, J. B.; Plis, E.; Bishop, G.; Sharma, Y. D.; Kim, H.; Dawson, L. R.; Krishna, S. NBN Structure Based on InAs/GaSb Type-II Strained Layer Superlattices. *Appl. Phys. Lett.* **2007**, *91*, 043514.

(21) Hafiz, S. B.; Al Mahfuz, M. M.; Scimeca, M. R.; Lee, S.; Oh, S. J.; Sahu, A.; Ko, D.-K. Ligand Engineering of Mid-Infrared Ag₂Se Colloidal Quantum Dots. *Phys. E Low-Dimens. Syst. Nanostruct.* **2020**, *124*, 114223.

(22) Ko, D.-K.; Brown, P. R.; Bawendi, M. G.; Bulović, V. P-i-n Heterojunction Solar Cells with a Colloidal Quantum-Dot Absorber Layer. *Adv. Mater.* **2014**, *26*, 4845–4850.

(23) Saran, R.; Curry, R. J. Lead Sulphide Nanocrystal Photodetector Technologies. *Nat. Photonics* **2016**, *10*, 81–92.

(24) Carey, G. H.; Abdelhady, A. L.; Ning, Z.; Thon, S. M.; Bakr, O. M.; Sargent, E. H. Colloidal Quantum dot Solar Cells. *Chem. Rev.* **2015**, *115*, 12732–12763.

(25) Pradhan, S.; Di Stasio, F.; Bi, Y.; Gupta, S.; Christodoulou, S.; Stavrinadis, A.; Konstantatos, G. High-Efficiency Colloidal Quantum Dot Infrared Light-Emitting Diodes via Engineering at the Supra-Nanocrystalline Level. *Nat. Nanotechnol.* **2019**, *14*, 72–79.

(26) Sahu, A.; Khare, A.; Deng, D. D.; Norris, D. J. Quantum Confinement in Silver Selenide Semiconductor Nanocrystals. *Chem. Commun.* **2012**, *48*, 5458–5460.

(27) Evans, C. M.; Evans, M. E.; Krauss, T. D. Mysteries of TOPSe Revealed: Insights into Quantum Dot Nucleation. *J. Am. Chem. Soc.* **2010**, *132*, 10973–10975.

(28) Steckel, J. S.; Yen, B. K. H.; Oertel, D. C.; Bawendi, M. G. On the mechanism of Lead Chalcogenide Nanocrystal Formation. *J. Am. Chem. Soc.* **2006**, *128*, 13032–13033.

(29) Hines, M. A.; Scholes, G. D. Colloidal PbS Nanocrystals with Size-Tunable Near-Infrared Emission: Observation of Post-Synthesis Self-Narrowing of the Particle Size Distribution. *Adv. Mater.* **2003**, *15*, 1844–1849.

- (30) Talapin, D. V.; Lee, J.-S.; Kovalenko, M. V.; Shevchenko, E. V. Prospects of Colloidal Nanocrystals for Electronic and Optoelectronic Applications. *Chem. Rev.* **2010**, *110*, 389–458.
- (31) Luther, J. M.; Law, M.; Song, Q.; Perkins, C. L.; Beard, M. C.; Nozik, A. J. Structural, Optical, and Electrical Properties of Self-Assembled Films of PbSe Nanocrystals Treated with 1,2-Ethanedithiol. *ACS Nano* **2008**, *2*, 271–280.
- (32) Son, K.-A.; Wong, D.; Sharifi, H.; Seo, H. C.; De Lyon, T.; Terterian, S.; Moon, J. S.; Hussain, T. Silver Nanowire-Based Infrared-Transparent Contacts for Future High-Density Format Focal Plane Arrays. *IEEE Trans. Nanotechnol.* **2015**, *14*, 10–14.
- (33) Zhang, R.; Engholm, M. Recent Progress on the Fabrication and Properties of Silver Nanowire-Based Transparent Electrodes. *Nanomaterials* **2018**, *8*, 628.
- (34) Robin, A.; Livache, C.; Ithurria, S.; Lacaze, E.; Dubertret, B.; Lhuillier, E. Surface Control of Doping in Self-Doped Nanocrystals. *ACS Appl. Mater. Interfaces* **2016**, *8*, 27122–27128.
- (35) Jasieniak, J.; Califano, M.; Watkins, S. E. Size-Dependent Valence and Conduction Band-Edge Energies of Semiconductor Nanocrystals. *ACS Nano* **2011**, *5*, 5888–5902.
- (36) Gao, J.; Luther, J. M.; Semonin, O. E.; Ellingson, R. J.; Nozik, A. J.; Beard, M. C. Quantum Dot Size Dependent J - V Characteristics in Heterojunction ZnO/PbS Quantum Dot Solar Cells. *Nano Lett.* **2011**, *11*, 1002–1008.
- (37) Wuesten, J.; Ziegler, C.; Ertl, T. Electron Transport in Pristine and Alkali Metal doped Perylene-3,4,9,10- Tetracarboxylicdianhydride (PTCDA) Thin Films. *Phys. Rev. B: Condens. Matter Mater. Phys.* **2006**, *74*, 125205.
- (38) Konstantatos, G.; Sargent, E. H. Solution-Processed Quantum Dot Photodetectors. *Proc. IEEE* **2009**, *97*, 1666–1683.
- (39) Baumgardner, W. J.; Whitham, K.; Hanrath, T. Confined-But-Connected Quantum Solids via Controlled Ligand Displacement. *Nano Lett.* **2013**, *13*, 3225–3231.
- (40) Mentzel, T. S.; Porter, V. J.; Geyer, S.; MacLean, K.; Bawendi, M. G.; Kastner, M. A. Charge Transport in PbSe Nanocrystal Arrays. *Phys. Rev. B: Condens. Matter Mater. Phys.* **2008**, *77*, 075316.
- (41) Yu, D.; Wang, C.; Wehrenberg, B. L.; Guyot-Sionnest, P. Variable Range Hopping Conduction in Semiconductor Nanocrystal Solids. *Phys. Rev. Lett.* **2004**, *92*, 216802.
- (42) Kang, M. S.; Sahu, A.; Norris, D. J.; Frisbie, C. D. Size- and Temperature-Dependent Charge Transport in PbSe Nanocrystal Thin Films. *Nano Lett.* **2011**, *11*, 3887–3892.
- (43) Guyot-Sionnest, P. Electrical Transport in Colloidal Quantum Dot Films. *J. Phys. Chem. Lett.* **2012**, *3*, 1169–1175.
- (44) Tang, X.; Ackerman, M. M.; Guyot-Sionnest, P. Thermal Imaging with Plasmon Resonance Enhanced HgTe Colloidal Quantum Dot Photovoltaic Devices. *ACS Nano* **2018**, *12*, 7362–7370.
- (45) Guyot-Sionnest, P.; Roberts, J. A. Background Limited Mid-Infrared Photodetection with Photovoltaic HgTe Colloidal Quantum Dots. *Appl. Phys. Lett.* **2015**, *107*, 253104.
- (46) Chen, M.; Lan, X.; Tang, X.; Wang, Y.; Hudson, M. H.; Talapin, D. V.; Guyot-Sionnest, P. High Carrier Mobility in HgTe Quantum Dot Solids Improves Mid-IR Photodetectors. *ACS Photonics* **2019**, *6*, 2358–2365.
- (47) Livache, C.; Martinez, B.; Goubet, N.; Gréboval, C.; Qu, J.; Chu, A.; Royer, S.; Ithurria, S.; Silly, M. G.; Dubertret, B.; Lhuillier, E. A Colloidal Quantum Dot Infrared Photodetector and Its Use for Intrapband Detection. *Nat. Commun.* **2019**, *10*, 2125.